Journal of Energetic Materials
Publication details, including instructions for authors and subscription information:
http://www.informaworld.com/smpp/title~content=t713770432

A Multifield Model and Method for Metal-Loaded High Explosives

B. A. Kashiwa[a]; L. M. Hull[a]
[a] Los Alamos National Laboratory, Los Alamos, New Mexico, USA

Online publication date: 15 October 2010

To cite this Article Kashiwa, B. A. and Hull, L. M.(2010) 'A Multifield Model and Method for Metal-Loaded High Explosives', Journal of Energetic Materials, 28: 1, 16 — 34
To link to this Article: DOI: 10.1080/07370651003776991
URL: http://dx.doi.org/10.1080/07370651003776991

Journal of Energetic Materials, 28: 16–34, 2010

ISSN: 0737-0652 print/1545-8822 online
DOI: 10.1080/07370651003776991

Taylor & Francis
Taylor & Francis Group

A Multifield Model and Method for Metal-Loaded High Explosives

B. A. KASHIWA and L. M. HULL

Los Alamos National Laboratory, Los Alamos, New Mexico, USA

An ensemble average of the full conservation equations for multiple materials produces an unclosed system called the multifield equations. Closures are approached by way of correlation to data from direct numerical simulations or from experiment for simplified conditions. The resulting multifield model using this approach is displayed and a numerical solution method used for sample simulations is outlined. Selected results are shown to illustrate the utility of the model and method for understanding the performance of a high explosive with a dense loading of small tungsten grains.

Keywords: equation-of-state (EOS), high-explosive (HE), metal-loaded, multifield

Introduction

We present a summary of ongoing work whose goal is to devise a predictive modeling capability for extremely nonideal high explosives and for their performance during warhead disassembly and target interaction. A multifield approach is used, that considers the averaged interaction of multiple separated

Address correspondence to Dr. Bryan A. Kashiwa, Los Alamos National Laboratory, Theoretical Division, B216, Los Alamos, NM 87545, USA. E-mail: bak@lanl.gov

materials. For each material the complete equation of state (EOS) and material response function are assumed to be known. An ensemble average of the conservation laws produces continuum equations for each material; these are called the *multifield* equations. Closure relations for exchanges of mass, momentum, and energy among fields are obtained by correlation to data generated either by direct numerical simulation or by experiment, for conditions chosen to isolate certain terms in the equations. For the studies of interest so far, as in the examples discussed here, the effects of turbulence have been neglected. Numerical solutions are computed using a finite-volume discretization scheme that permits integration of each field state in either the Lagrangian frame or the Eulerian frame of reference. Either frame can be chosen for any material field in the problem, so the method is called a *mixed-frame* approach.

Model and Closures

Development of the multifield continuum equations used for these studies has been described elsewhere [1]. That development is summarized here. The equations arise from a straightforward ensemble averaging procedure applied to a closed set of conservation laws for any pure material whose EOS and material response are given. By considering N *separated* materials, the averaging produces N sets of equations for the conservation of mass, linear momentum, and energy. These fieldwise conservation laws are unclosed as a result of the averaging: closures for the volume fraction, turbulence, and exchanges of mass, momentum, and energy among fields are required. For the volume fraction closure, we assume pressure equilibrium. Hence, this is a continuum model with thermal and velocity nonequilibrium and, when appropriate, a complete history-dependent material stress.

Using the subscript r to signify the field number ($r = 1, 2, \ldots, N$), the thermodynamic state is given by the r mass, velocity, total energy, specific volume, and stress $[M_r, \mathbf{u}_r, E_r, v_r, \sigma_r]$. In an arbitrary volume V, the r density is then $\rho_r(\mathbf{x},t) = M_r/V$ and the sum on r is the total mass density at a space–time point

$(\mathbf{x},\ t)$. The derivative along the r motion is $D_r()/Dt = \partial()/\partial t + \mathbf{u}_r \cdot \boldsymbol{\nabla}()$, and the model equations are

$$\frac{1}{V}\frac{D_r M_r}{Dt} = \sum_{s=1}^{N} \Gamma_{rs} = \Gamma_r \tag{1}$$

$$\frac{1}{V}\frac{D_r(M_r \mathbf{u}_r)}{Dt} = \sum_{s=1}^{N} \mathbf{u}_{rs}^{+}\Gamma_{rs} - \theta_r \nabla p + [\nabla \cdot \theta_r \bar{\boldsymbol{\sigma}}_r] - \nabla \cdot \rho_r \mathbf{R}_r + \rho_r \mathbf{g} + \mathbf{f}_r \tag{2}$$

$$\frac{1}{V}\frac{D_r(M_r E_r)}{Dt} = \frac{1}{V}\frac{D_r(M_r e_r)}{Dt} + \frac{1}{V}\frac{D_r\left(M_r \frac{1}{2} u_r^2\right)}{Dt} - \rho_r \mathbf{u}_r \cdot \mathbf{g} \tag{3a}$$

$$\frac{1}{V}\frac{D_r(M_r e_r)}{Dt} = \sum_{s=1}^{N} \hat{\mu}_{rs}\Gamma_{rs} + [\theta_r \boldsymbol{\sigma}_r : \boldsymbol{\nabla} u_r] - \boldsymbol{\nabla} \cdot \mathbf{j}_r + q_r + \rho_r \varepsilon_r - \frac{p}{V}\frac{D_r(M_r v_r)}{Dt} \tag{3b}$$

$$\frac{1}{V}\frac{D_r(M_r v_r)}{Dt} = \left[v_r \Gamma_r - f_r^{\theta} \sum_{s=1}^{N} v_s \Gamma_s\right] + \left[\theta_r \beta_r \frac{D_r T_r}{Dt} - f_r^{\theta} \sum_{s=1}^{N} \theta_s \beta_s \frac{D_s T_s}{Dt}\right] + f_r^{\theta} \boldsymbol{\nabla} \cdot \mathbf{u} \tag{3c}$$

$$\hat{\boldsymbol{\sigma}}_r = \Phi_r[\mathbf{F}_r,\ \boldsymbol{\sigma}_r, \boldsymbol{\nabla}\mathbf{u}_r, *_r] \tag{4}$$

$$\theta_r = \rho_r v_r \tag{5}$$

$$0 = 1 - \sum_{s=1}^{N} \rho_s v_s \tag{6}$$

$$e_r = \tilde{e}_r(v_r, T_r) \tag{7}$$

$$p = \tilde{p}_r(v_r, T_r) \tag{8}$$

where the nomenclature is, in order of appearance,

Γ_{rs} = volumetric rate of r-s mass exchange ($\Gamma_{rs} + \Gamma_{sr} = 0$) ($c1$)
u_{rs}^{+} = mean velocity of the field "donating" mass to field r ($\mathbf{u}_{rs}^{+} = \mathbf{u}_{sr}^{+}$)
p = isotropic mean stress ($\boldsymbol{\sigma} = -p\mathbf{I}$)
$\bar{\boldsymbol{\sigma}}_r$ = r-field stress, relative to the mean stress ($\bar{\boldsymbol{\sigma}}_r = \boldsymbol{\sigma}_r - \boldsymbol{\sigma}$)
$-\rho_r \mathbf{R}_r$ = r-field Reynolds stress density ($c2$)
$\mathbf{f}_r$ = r-field force density due to interactions with all other fields in V ($c3$)
e_r = r-field specific internal energy $\left(e_r = E_r - \frac{1}{2} u_r^2\right)$
$\hat{\boldsymbol{\mu}}_{rs}$ = enthalpy of formation associated with r-s conversion ($\hat{\boldsymbol{\mu}}_{rs} = \hat{\boldsymbol{\mu}}_{sr}$)
$-\mathbf{j}_r$ = r-field heat flux due to both conduction and fluctuational transport ($c4$)
T_r = r-field temperature
q_r = rate of r-field heat exchange with all other fields in V ($c5$)
$\rho_r \varepsilon_r$ = dissipation rate of r-field turbulence energy ($c6$)
v_r = specific volume of r-field material
$f_r^{\theta} = \theta_r \kappa_r / \sum_{s=1}^{N} \theta_s \kappa_s$: a positive fraction between zero and one
$\kappa_r = -[\partial v_r / \partial p] / v_r$: constant temperature compressibility of r-field material
$\beta_r = [\partial v_r / \partial T] / v_r$: constant pressure volumetric expansivity of r-field material
$\mathbf{u} = \sum_{s=1}^{N} \theta_s \mathbf{u}_s$: total volume flux
$\boldsymbol{\Phi}_r$ = response function for r material stress, due to r-field straining

and where the items numbered ($c1$–$c6$) require closure models; everything else is a known function of the state or a property of the pure r-field material.

For a solid material the stress satisfies an evolution equation, given symbolically by Eq. (4), where the overhat signifies the rate of stress change in polar axes. The symbol $\boldsymbol{\Phi}_r$ is the general material response function that may depend on the deformation

gradient $\mathbf{F}_r$, the r stress itself, the averaged r-field rate of strain and a list of items indicated by the $*_r$, which may include history variables such as a damage parameter, as well as the rotation of the polar axes relative to spatial coordinates. For a fluid material, $\boldsymbol{\sigma}_r = -p\boldsymbol{I} + \boldsymbol{\tau}_r$, where the deviatoric stress is the Newtonian one (and Eq. (4) is omitted for that field).

The temperature T_r, specific volume v_r, volume fraction θ_r, and pressure p are all quantities related to the r mass density $\rho_r = M_r/V$ and r-specific internal energy e_r, by way of equations-of-state (EOS). Equations (7) and (8) are, respectively, the caloric equation of state and the thermal (EOS), signified by the overtilde. Equation (5) *defines* the the volume fraction, θ_r, and with that definition, Eq. (6) follows. We refer to Eqs. (6)–(8) as the multifield equation of state. The pressure is the one value of p that permits arbitrary masses of the materials to occupy the entirety of the volume V (for this reason it has been called the *equilibration* pressure). Hence, the volume fractions are determined by the multifield equation of state. Equation (3c) is the volume rate consistent with Eqs. (6)–(8).

In our studies we use EOS data from the SESAME database [2] or the simpler analytic forms used by Mader [3]; further, we neglect the effects of turbulence and the heat flux $\mathbf{j}_r$ by assuming that mass exchange ($c1$), momentum exchange ($c3$), and heat exchange ($c5$) represent the dominant physics. The mass exchange rate is the high-explosive (HE) burn rate, which is assumed to be the rate for pure HE 9404 using the forest fire model reported by Mader [3]. This assumption considers the HE burn rate to be a property of the pure r-field material taken in isolation, a postulate that is to be verified by comparison to experimental data. The momentum and heat exchange rates are found by correlation to direct numerical simulation, as described by Kashiwa and Hull [1].

Numerical Solution Method

Equations (1)–(4) describe the physical changes to the matter that resides, momentarily, in an arbitrary volume of space; these are called the *Lagrangian rate equations* for multiple

fields. For each field, the volume, although arbitrary in size and shape, moves along the mean trajectory $\mathbf{u}_r$. For N fields there are N separate trajectories, representing N different material frames of reference. These Lagrangian changes must all be reconciled to a common frame of reference, in order to satisfy the conservation principles for system mass, system linear momentum, and system total energy. (In other words, the equations must be summable over all fields, which requires a common frame.) Therefore, a coordinate transformation is needed, and one that is frequently used is called the *generalized Reynolds transport theorem*. Let $\mathbf{u}_g$ be the trajectory of a common reference frame, and let Q_r be any of the total quantities in V with q_r signifying its density. The theorem is

$$\frac{D_g Q_r}{Dt} + \int_V \left[\nabla \cdot q_r(\mathbf{u}_r - \mathbf{u}_g)\right] dV = \frac{D_r Q_r}{Dt}, \tag{9}$$

in which we typically assume that the gradient is constant in the volume V. Equation (9) relates the change in any total quantity Q_r, in a volume moving with velocity $\mathbf{u}_g$, to the rate of change along the r-field motion $\mathbf{u}_r$. The difference between the two rates is the second term on the left, called the *advection* term. Equation (9) is valid, as long as the r-Lagrangian volume and the volume moving with $\mathbf{u}_g$ are precisely overlapping at the instant for which the evaluation is made.

In each grid cell, we use a numerical method for solving Eqs. (1)–(9) that is split relative to the Lagrangian and transport parts of the model equations [4]. First, for all fields, the Lagrangian changes are computed at each grid location using state data that are in grid coordinates. This is called the *Lagrangian phase of the time–split calculation*. Second, the transport changes are evaluated; this is called the *transport phase*.

We employ two options for transport, which can be selected on a field-by-field basis. One option is called *Eulerian*, for which a discrete form of Eq. (9) is evaluated; in this case the primitive state data are stored in grid coordinates. The other option is called *Lagrangian*, in which case the full thermodynamic state

is stored on ''markers'' that move with the center-of-mass motion of the field. Each marker is a finite element of r mass whose motion is determined by the r-field conservation equations. (Frequently the aggregate behavior of a collection of markers is that of a solid body, submerged in a fluid whose transport is Eulerian. In this case the simulation is one of a fluid structure interaction.) When the Lagrangian option is used for a field, the state must be interpolated from marker coordinates to grid coordinates, in order to evaluate the state variables and in order to evaluate the Lagrangian changes (in the first phase

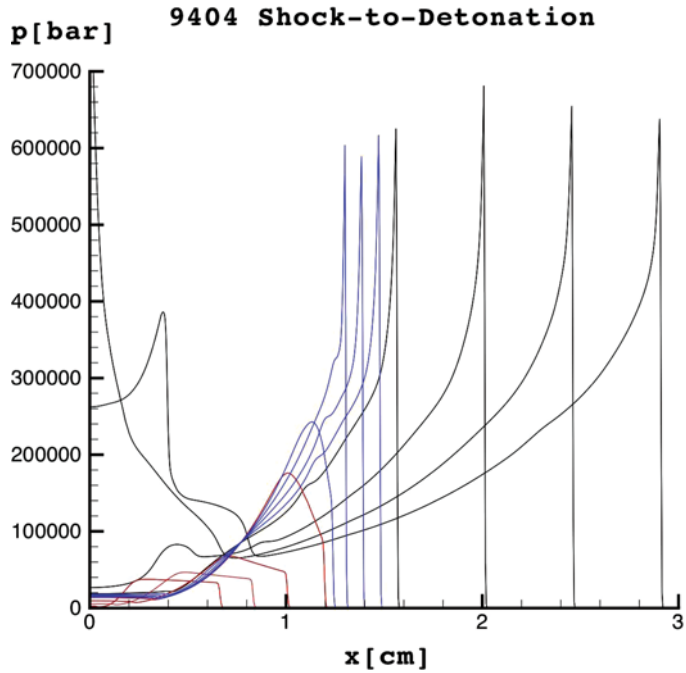

Figure 1. Shock-to-detonation calculation for explosive 9404 in 1D. Pressure vs. distance at various times for initiation by a 30 kbar shock in unburned material at $x < 0.5$ cm. Wave moves to the right. Red lines are for times $t = (0.5, 1.0, 1.5, 2.0)$ μs; blue are for $t = (2.1, 2.2, 2.3, 2.4)$ μs; black are for $t = (2.5, 3.0, 3.5, 4.0)$ μs. The steady detonation speed of 890 cm/ms is to be compared to the measured value of 880 cm/ms.

of the calculation); in this way, Eulerian advection is traded for an interpolation.

Example Simulations

To illustrate the model and associated numerical solution method, we first present 1D results for explosive 9404 (plastic-bonded cyclotetramethylenetetranitramine (HMX) [3]), and then we focus on a well-characterized HE known as X0233 [3], which consists of HMX grains bonded in a plastic matrix along with a heavy mass loading of small tungsten grains. These examples are chosen in order to show, in a progressive manner, the utility of the simulations for understanding the behavior of these explosives.

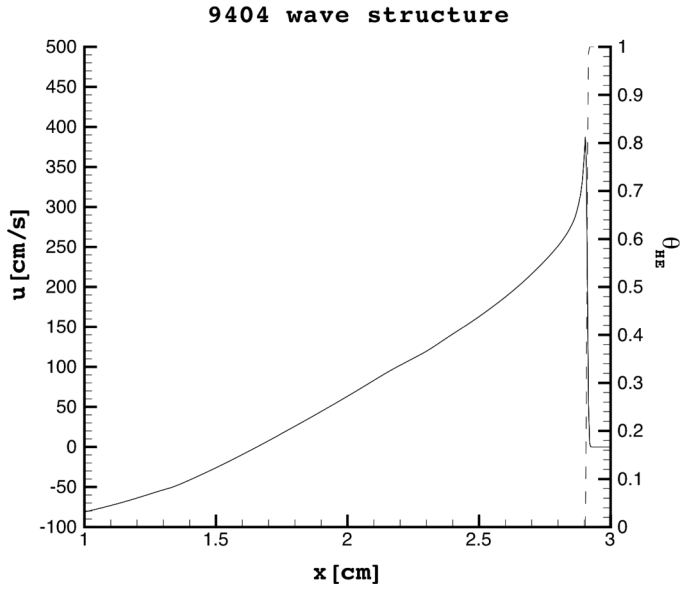

Figure 2. Steady detonation wave structure for explosive 9404 in 1D. Velocity and volume fraction of unburned HE vs. distance, at a time of 4.0 μs. Solid line is velocity; dashed line is HE volume fraction. Width of the burn zone is approximated by about three computational cells, or 0.012 cm.

Figure 1 shows pressure vs. distance for a 1D shock-to-detonation calculation for explosive 9404. In this, two material fields are used: (1) unburned HE and (2) products of combustion. Burn rate and EOS models are all those given by Mader [3], from which the burn rate is 9404 forest fire; Mie-Grüneisen (HOM) EOS is used for the HE; and a Becker-Kistiakowski-Wilson (BKW) EOS is used for the products of combustion, assuming complete decomposition. Initiation is caused by a 0.5 cm slug of material at Hugoniot conditions associated with HE shocked to 30 kbar relative to HE at one bar. The grid cell

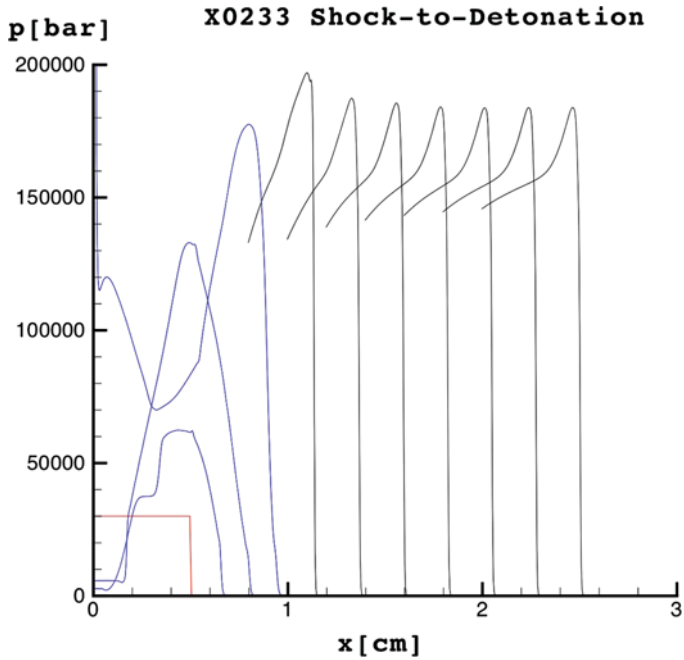

Figure 3. Shock-to-detonation calculation for explosive X0233 in 1D. Pressure vs. distance at various times for initiation by a 30 kbar shock in unburned material at $x < 0.5$ cm. Wave moves to the right. Red line is for time $t = 0.0$; blue is for $t = (0.5, 1.0, 1.5)$ μs; black is for $t = (2.0, 2.5, 3.0, 3.5, 4.0, 4.5, 5.0)$ μs. The steady detonation speed of 460 cm/ms is to be compared to the measured value of 451 cm/ms.

size is $\Delta x = 0.004$ cm. In Fig. 1 the apparent distance to detonation is about 0.8 cm, which is consistent with the data used to establish the burn rate using the forest fire model [3]. Figure 2 shows the wave structure, which indicates a burn zone thickness that is of the order of three grid cells, and a standard Taylor wave expansion. Hence, the solutions are consistent with the closure data used for EOS and burn rate.

Figure 3 shows pressure vs. distance for a 1D shock-to-detonation simulation for explosive X0233 [3], modeled using all of the same parameters used for the 9404 calculation plus a 35% volume loading of tungsten grains having an averaged diameter

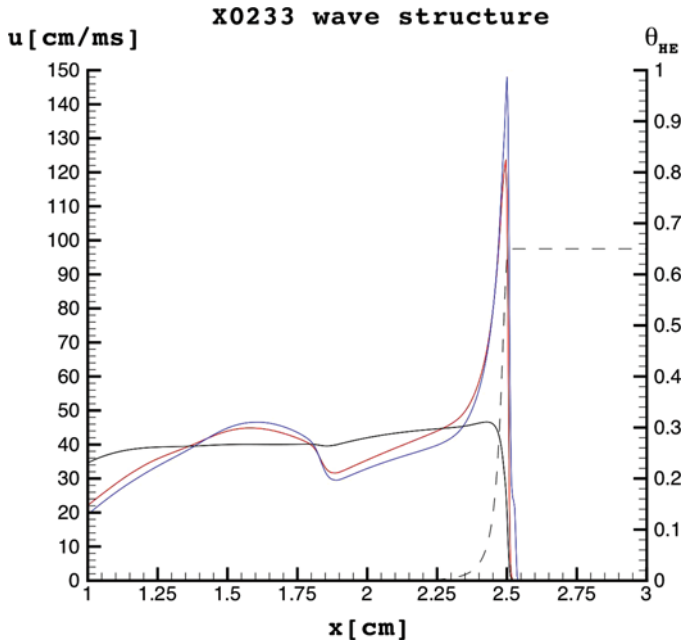

Figure 4. Steady detonation wave structure for explosive X0233 in 1D. Velocity and volume fraction of unburned HE vs. distance, at a time of 5.0 μs. Solid lines are velocity: red is for HE, blue is for products of combustion, black is for tungsten grains; dashed line is HE volume fraction. Width of the burn zone is approximately 0.2 cm.

of 30 μm. Hence, the only difference is the addition of a massive material (treated as inert) that occupies a significant portion of the volume. Thus, there are now three material fields: (1) unburned HE, (2) products of combustion, and (3) tungsten grains. This figure shows that addition of the tungsten results in a slightly shortened run to detonation but a significantly slower wave speed and lower pressure compared to 9404 without tungsten loading. Figure 4 has the X0233 wave structure, which is characterized by a significantly flattened Taylor wave expansion, the reason for which is clearly the high inertia of the tungsten grains, which exhibit a nearly constant velocity behind the burn wave.

For a two-dimensional illustration we show simulation results for an experiment designed to measure the separation of tungsten grains from the products of combustion in X0233. Figure 5 depicts a brick of X0233 supported in air by Lexan and steel

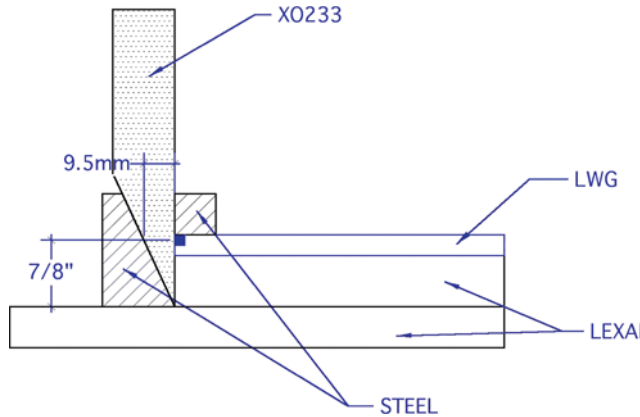

Figure 5. Assembly drawing for the X0233 burn experiment. A brick of X0233 with a wedge-shaped nose is supported by Lexan and steel; a line wave generator (LWG) causes initiation along the full depth of the brick just below the square steel support. The experiment was conducted in room temperature air at about 0.8 bar. Both optical and radiographic images were taken at multiple times in order to track the progress of the tungsten grains and of the products of combustion.

blocking. Initiation is by means of a line wave generator (LWG). Both optical and radiographic imaging were used in order to track the progress of the tungsten and of the forward edge of the combustion products. These images showed that the front of the tungsten grains forms an angle of 21.6 degrees with the brick vertical surface and the products form an angle of 44.0 degrees. In addition, an aluminum witness plate was stationed on an angle relative to the brick side, and velocity interferometer system for any reflector (VISAR) was used to measure changes in position of the plate (and thereby the plate velocity).

We computed the X0233 burn on the grid shown in Fig. 6, with the same input parameters used for the 1D X0233 shock-to-detonation shown previously, except initiation assumed a

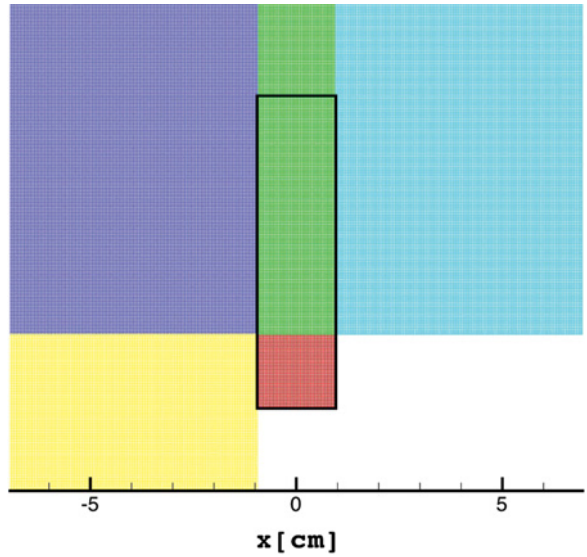

Figure 6. 2D multiblock grid used for calculation of X0233 brick experiment. Colors indicate the five blocks; black line indicates location of the X0233 brick. A free-slip boundary separates the red and yellow blocks. Initiation is by a 100 kbar shock in the lower left corner of the red block, moving to the left. Grid cells are $\Delta x = \Delta y = 0.05$ cm.

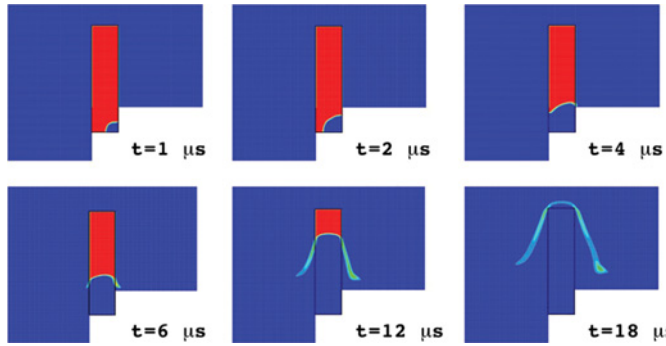

Figure 7. Time sequence of the 2D burn calculation for X0233. Contours of HE volume fraction. A thin layer of unburned HE is ejected from the lateral surface of the brick. The detonation wave speed up the brick is 460 cm/ms and is consistent with both data and the fine-zoned 1D calculations.

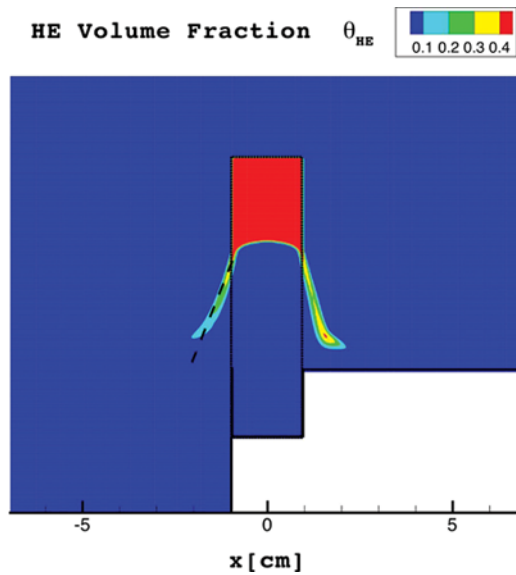

Figure 8. HE volume fraction for 2D X0233 burn calculation, at a time of 11 μs. Dashed line delineates the lateral progress of the tungsten grains, inferred from the radiographic data.

100 kbar shock from the LWG, and we used a coarser grid spacing. In this, we assumed that the surrounding air has the same EOS as the combustion products so that there are still three material fields. Figure 7 shows a time sequence of HE volume fraction contours, indicating the general progress of the burn. Despite a nonsymmetric initiation, the burn rapidly becomes fairly symmetric after progressing above the steel blocking. Figure 8 has HE volume fraction with the measured tungsten front indicated by a dashed line; Fig. 9 shows tungsten volume fraction at the same time. These figures indicate that the model and method accurately capture the tungsten motion.

The simulation also reveals that a layer of poorly burned HE is ejected laterally from the brick. This suggests that if the width of the brick was to be made comparable to the thickness of the ejected layer, the detonation may fail; hence, we expect

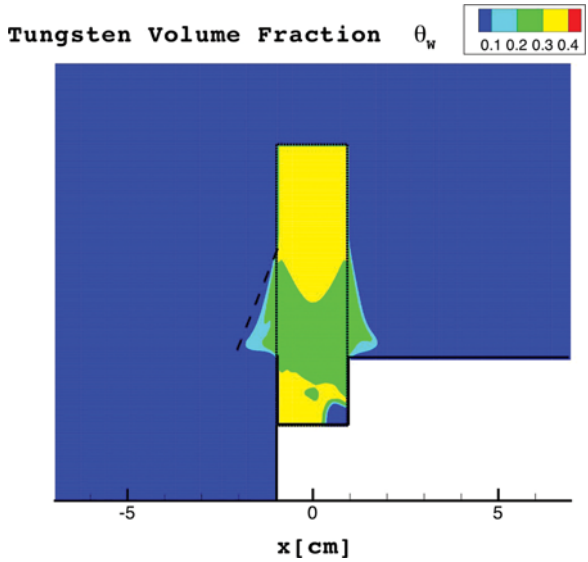

Figure 9. Tungsten volume fraction for 2D X0233 burn calculation, at a time of 11 μs. Same dashed line as in Fig. 8 shows that the tungsten does not progress beyond the unburned layer.

that this type of calculation would reproduce the so-called failure diameter found in rate stick experiments for this explosive.

Figure 10 shows contours of pressure using a logarithmic scale, in order to estimate the lateral progress of the combustion products. Here it is seen that the overall progress is captured well, but there exists a structure in the pressure wave that is not seen in the experiments. We find that this discrepancy is mainly due to the equations of state assumed for the products of combustion; subsequent studies using SESAME [2] nitrogen to model the products (and the air) produce a flat pressure wave.

Figures 11 and 12 show the simulation of Fig. 10 repeated using SESAME EOS data for all materials. For this we also add a fourth material in order to show the explosive impact

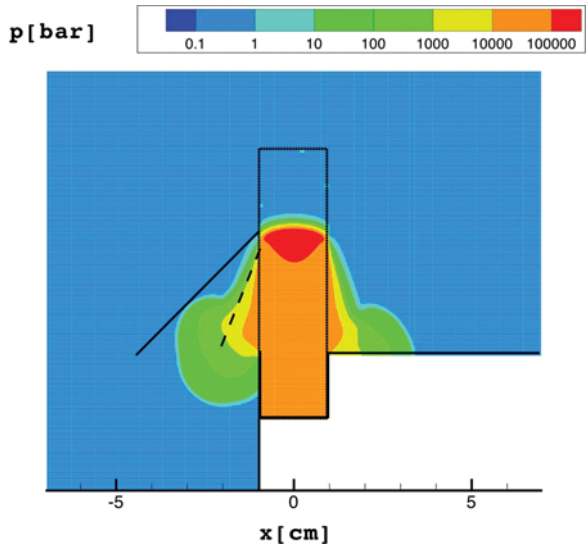

Figure 10. Pressure contours for 2D X0233 burn calculation at a time of 11 μs. Same dashed line as in Fig. 8. Solid black line indicates the lateral progress of combustion products inferred from optical images of the experiment, which appears to be a turbulent mixing front.

with the aluminum witness plate. Now we consider four material fields: (1) HE, (2) products (modeled as nitrogen), (3) tungsten, and (4) aluminum (witness plate). Here we use the same 9404 forest fire burn rate, and we represent the aluminum plate in the Lagrangian frame of reference. Furthermore, we solve a reduced momentum equation, called the *plate equation* [5], for the motion of the aluminum whose thickness is comparable to the grid spacing. This permits us to resolve the plate motion including the response to torque loading (moments), and it removes the problem of resolving wave motions within the thickness of the plate. Using the plate equation option allows resolution of the witness plate with a single layer of Lagrangian mass markers. Figure 11 shows a flattened

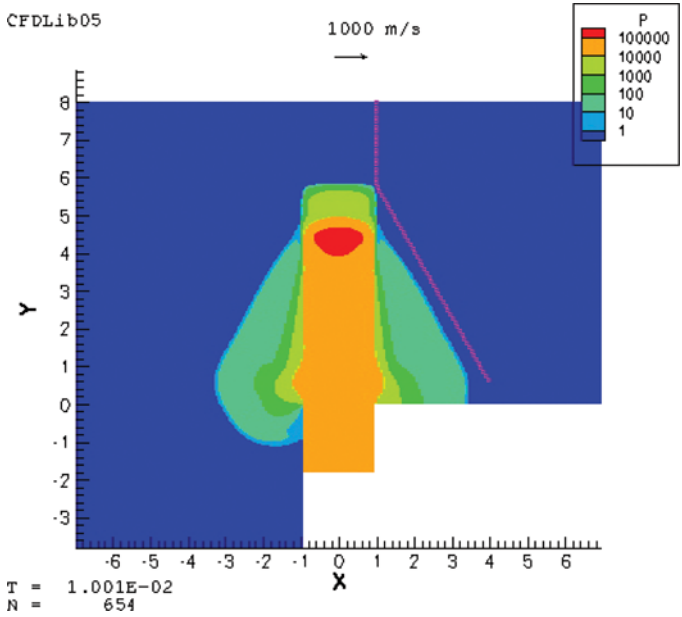

Figure 11. Pressure contours for the 2D X0233 burn calculation, repeated using SESAME EOS data. Symbols represent Lagrangian mass marker locations for the aluminum witness plate.

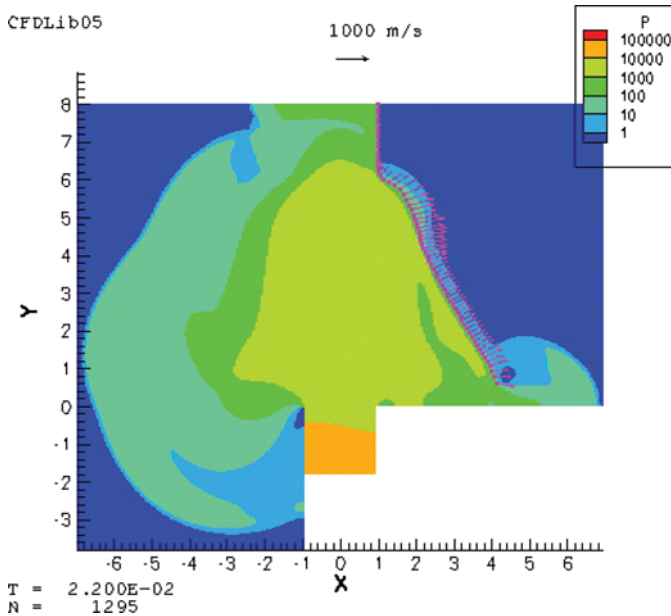

Figure 12. Pressure contours for 2D X0233 burn calculation, repeated using SESAME EOS data. Symbols represent Lagrangian mass marker locations for the aluminum witness plate. Vectors represent marker velocity.

pressure wave that is a result of using more accurate EOS data; Fig. 12 shows a later time, after the explosive products have accelerated the witness plate. Figure 13 contains a comparison of the computed velocity of the witness plate near its lower edge, with VISAR measurements near the same location. This shows good agreement with the plate acceleration; the timing difference is mainly due to a lack of taper (wedge) on the simulated brick. (Note that the detonation wave speed and structure are incorrect in this calculation because the EOS used are different than those used to determine the forest fire burn rate, which goes hand in hand with the EOS. Another burn rate that is consistent with the SESAME EOS data, and with the 9404 shock-to-detonation distance

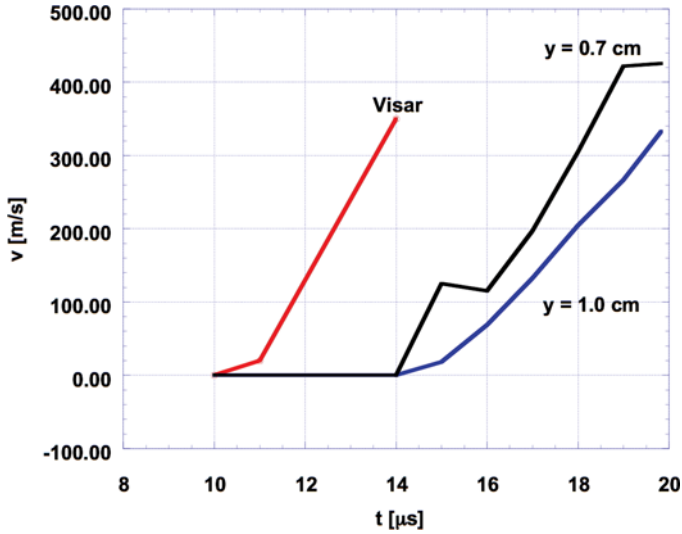

Figure 13. Velocity of the aluminum witness plate vs. time. Red line is the experimental VISAR measurement; black and blue lines indicate the computed velocity at two different plate locations near the location of the VISAR measurement. Timing offset is due mainly to the lack of a taper (wedge) on the simulated brick.

data, is yet to be determined according to the procedure given by Mader [3].)

Conclusion

We conclude that the modeling approach and the numerical solution method used has potential merit for warhead design and prediction of warhead target interactions. Future work of interest includes application to fuel–air explosives for which turbulence effects are typically nonnegligible, as well as HE loaded with reactive metals, which may decompose after passage of the detonation wave. In these and other cases, the predictive nature of the model is expected to be valuable for scoping the performance of conceptual HE systems; that is, those that are as yet untested.

Acknowledgment

Los Alamos National Laboratory is operated by Los Alamos National Security LLC, for the U.S. Department of Energy's NNSA. Support for this work by the DOE/DoD Joint Munitions Program is gratefully acknowledged.

References

[1] Kashiwa, B. A. and L. M. Hull. 2004. Multifield closure modeling for metal-loaded high explosives (U). *7th Joint Classified Bombs/ Warheads & Ballistics Symposium*, National Defense Industrial Association, Monterey, CA, 9–12 August 2004. King of Prussia, PA: D. E. Technologies, Inc.

[2] Holian, K. S., ed. 1984. *T-4 Handbook of Material Properties Data Bases: Vol. Ic. Equations of State*. Los Alamos National Laboratory report LA–10160–MS. Los Alamos, CA: University of California.

[3] Mader, C. L. 1998. *Numerical Modeling of Explosives and Propellants*. New York: CRC Press LLC.

[4] Kashiwa, B. A. and E. S. Gaffney. 2003. *Design Basis for CFDLib*. Los Alamos National Laboratory document LA-UR-03-1295. Los Alamos, CA: University of California.

[5] Kashiwa, B. A. and M. W. Lewis. 1998. *Fluid-Structure Interaction Modeling*. Los Alamos National Laboratory Report LA-13415-PR. Los Alamos, CA: University of California.